Original Research

Evaluation of pulmonary response to inhaled tungsten (IV) oxide nanoparticles in golden Syrian hamsters

Milankumar V Prajapati[1], Olujoba O Adebolu[1], Benjamin M Morrow[2] and Joseph M Cerreta[1]

[1]College of Pharmacy and Health Sciences, St. John's University, Queens, NY 11439, USA; [2]Materials Science & Technology, Los Alamos National Laboratory, Los Alamos, NM 87545, USA

Corresponding author: Joseph M Cerreta Email: cerretaj@stjohns.edu

Abstract

Extensive industrial and military uses of tungsten have raised the possibilities of human occupational and environmental exposure to nanoparticles of this metal, with concomitant health concerns. The goal of this study was to investigate the potential mechanism of pulmonary toxicity associated with inhaled tungsten (IV) oxide nanoparticles (WO_3 NPs) in Golden Syrian Hamsters. Animals exposed to WO_3 NPs via inhalation were divided into three groups — control and two treatment groups exposed to either 5 or 10 mg/m^3 of aerosolized WO_3 NPs for 4 h/day for four days. A long-term exposure study (4 h/day for eight days) was also carried out using an additional three groups. Pulmonary toxicity assessed by examining changes in cell numbers, lactate dehydrogenase activity, alkaline phosphatase activity, total protein content, TNF-α, and HMGB1 levels in bronchoalveolar lavage fluids showed a significant difference when compared to control ($P < 0.05$). The molecular mechanism was established by assessing protein expression of cathepsin B, TXNIP, NLRP3, ASC, IL-1β and caspase-1. Western blot analysis indicated a 1.5 and 1.7 fold changes in NLRP3 in treatment groups (5 mg/m^3, $P < 0.05$ and 10 mg/m^3, $P < 0.01$, respectively), whereas levels of cathepsin B were 1.3 fold higher in lung tissue exposed to WO_3 NPs suggesting activation of inflammasome pathway. Morphological changes studied using light and electron microscopy showed localization of nanoparticles and subsequent perturbation in airway epithelia, macrophages, and interstitial areas of alveolar structures. Results from the current study indicate that inhalation exposure to WO_3 NPs may induce cytotoxicity, morphological changes, and lung injury via pyroptotic cell death pathway caused by activation of caspase-1.

Keywords: Tungsten oxide, inhalation, nanoparticles, inflammasome

***Experimental Biology and Medicine* 2017; 242: 29–44. DOI: 10.1177/1535370216665173**

Introduction

Tungsten is a transition metal that occurs naturally in the earth's crust as oxides or salts and is widely used in military, industrial, and everyday applications. As a result of its properties (high density, strength, and stiffness), tungsten is a leading candidate for the production of military ammunitions replacing highly hazardous depleted uranium and lead.[1,2] Tungsten (IV) oxide nanoparticles (WO_3 NPs) are known to have excellent photochromic, electrochromic, gasochromic, and catalytic properties due to their large surface area.[3] Such properties make tungsten and its alloys indispensable. The concentration of tungsten particles in the ambient air is reported to be less than 10 ng/m^3.[4] However, inhalation exposure studies[5] indicate that the workplace concentration of dust in tungsten industries varies from 2.3 to 62.3 mg/m^3. Such increase in tungsten particulates occurs during milling, mining, and processing of tungsten ores and also during combustion of municipal waste.[6] Tungsten is used in manufacturing processes as a catalyst, pigment, and lubricants.[7] It is also used in the production of the fuel cell, solar panel, smart windows, and in dental fillings.[7] Such manufacturing processes may lead to the generation of particulate tungsten that is documented during manufacturing of metal alloys in the hard metal industry.[8,9] Moreover, the use of tungsten alloys in medical implants[10] may lead to generation of wear debris as seen with other metal alloys.[11] Owing to such applications, the risk of production of tungsten nanoparticles is high with a concomitant danger of respiratory tract injury following its inhalation. Further, increased use of tungsten may potentially contaminate surrounding air, water, and soil near tungsten mines and industrial sites.[6] Tungsten has been identified at several hazardous waste sites that have been proposed for inclusion on the environmental protection agency's (EPA) national priority list.[4]

Regulatory agencies from various countries (USA, Australia, Sweden, New Zealand, China) have issued regulatory guidelines with respect to tungsten exposure.[12] Currently, tungsten levels are not monitored routinely in the United States or Canada[13] and such monitoring is not known to be carried out by other countries. To date, with regard to tungsten, there are no drinking water guidelines issued by the WHO.[14] The current occupational exposure guidelines from the CDC's National Institute for Occupational Safety and Health (NIOSH) state that the recommended exposure levels (RELs) at a 10 h time-weighted average (TWA) for tungsten is 5 mg/m^3 and short-term exposure level (STEL) is 10 mg/m^3.[15] Until recently, tungsten alloys, with an exception of tungsten carbide,[16] have been considered relatively inert and hence not at significant risk of producing toxicity in humans. However, a recent study by Bolt *et al*.[13] has shown that tungsten enhances breast cancer metastasis as a result of its use in medical devices. In addition, earlier assessments were based on the physicochemical nature rather than toxicity that may be caused by small particle size. Although concerns about tungsten toxicity have been raised,[6,17,18] the respiratory toxicity of WO_3 NPs has yet to be investigated *in vivo* or *in vitro.* Due to lack of study in this field, very little is known about the toxicity of inhaled WO_3 NPs or the molecular mechanisms that may be involved in any toxicity.

Many studies involving nanoparticles utilize both *in vitro* or *in vivo* model system with *in vivo* models often using intra-tracheal instillation as a route of administration. However, such methods may not be appropriate to represent an occupational exposure scenario. Furthermore, Madl and Pinkerton[19] suggested that inhalation exposure provides a natural way of delivering toxicants and the associated deposition and clearance profiles of such materials are comparable to those seen in real world settings. Therefore, the current study utilized a whole body exposure chamber to assess the toxicity of WO_3 NPs.

Inflammasomes are molecular complexes located in the cell cytosol that are important intracellular signaling platforms, which detect pathogens and stressors and can activate highly pro-inflammatory cytokines, *i.e.* interleukin-1β (IL-1β) and IL-18.[20] Among the inflammasomes isotypes, the NLRP3 inflammasome is the most studied. The NLRP3 inflammasome consists of three main components[21]: 1 – the Nod-like receptor (NLR) family protein 3 (NLRP3); 2 – the adapter protein apoptosis-associated speck-like protein containing CARD (Caspase recruitment domain), termed as ASC or PYCARD; and 3 – procaspase-1, the precursor to the effector cysteine protease, caspase-1. Activation of NLRP3 may occur via the release of cathepsin B from lysosomes[22]; by the released ROS generated during oxidative stress via nanoparticles-induced injury leading to direct activation of NLRP3 inflammasome; or the ROS may activate thioredoxin-interacting protein (TXNIP) that in turn activates the NLRP3 inflammasomes.[23] Lysosomes contain many proteolytic proteins that upon activation are responsible for degrading cytosolic contents.[24] The cathepsin family of proenzymes is an important group of proteolytic proteins that are implicated in the activation of inflammasomes. Nanoparticles composed of titanium dioxide, silica, zinc oxide, copper oxide, or quantum dots are well known for generation of ROS[25] that can damage lysosomes and release their content. The release of lysosomal products can injure cells leading to cell death. Under normal condition, TXNIP (also known as VDUP, an activator of NLRP3) is constitutively bound and inactivated by the oxidoreductase thioredoxins (TRX). An increase in ROS production can lead to dissociation of complex TXNIP:TRX. The released TXNIP is then free to bind to NLRP3, activating the inflammasomes.[26] Such activation results in an inflammatory response and cell injury. Deposition of nanoparticles in the lysosomal compartment may ultimately result in lysosomal swelling and leakage of their contents, one of which is cathepsin B. Such release, in turn, may lead to the NLRP3 recruiting its adapter, ASC. The NLRP3 with its adapter then recruits pro-caspase-1 to undergo oligomerization forming the NLRP3 inflammasome. Pro-caspase-1 clustering on oligomerized NLRP3 results in its auto-activation to capspase-1. Activated caspase-1 may then process its cytoplasmic targets such as pro-IL-1β and pro-IL-18.[27] The release of these inflammatory mediators then can induce acute inflammation leading to cell injury. Alternatively, ruptured lysosomes may release their contents, promoting the mitochondrial production of oxidants.[26]

In the current study, a cellular mechanism for activation of inflammasome in pulmonary cells by WO_3 NPs is proposed. The central hypothesis of this research is that the inhalation of WO_3 NPs leads to their deposition in the airways, respiratory epithelium, and alveolar macrophages ultimately inducing cellular damage, pulmonary inflammation, and cytotoxicity via activation of the inflammasome.

Materials and methods

Materials

WO_3 NPs were purchased from Nanostructured & Amorphous Materials, Inc., (Houston, TX, USA). Nanosphere™ size standards, Pierce BCA® Protein Assay kit, PROTOCOL® HEMA 3 staining system, and Pierce™ Protease and phosphatase inhibitor were purchased from Thermo Fisher Scientific Inc., (Waltham, MA, USA). LDH Cytotoxicity Assay Kit and TNF-α EIA Kit were obtained from Cayman Chemicals Inc., (Ann Arbor, MI, USA). Alkaline phosphatase (ALP) Assay Kit was purchased from Abcam Inc., (Cambridge, MA, USA). Laemmli's sample buffer and non-fat dry milk were obtained from Bio-Rad Laboratories Inc., (Hercules, CA, USA). Amersham™ ECL™ Prime Western Blotting Detection Reagent was purchased from GE Healthcare UK Ltd, (Buckinghamshire, UK). Antibodies against NLRP3 (mAb), caspase-1 (mAb), IL-1β (mAb), and cathepsin B (pAb) were obtained from Cell Signaling Technology Inc., (Beverly, MA, USA). Antibodies against TXNIP (pAb) and β-actin (pAb) were purchased from Novus Biologicals LLC (Littleton, CO, USA). Antibody to HMGB1 (pAb) and ASC (pAb) were purchased from Sigma Aldrich Inc., (St. Louis, MO, USA) and Santa-Cruz Biotech Inc., (Dallas, TX, USA), respectively. Materials for microscopy such as 70% glutaraldehyde, sodium cacodylate, osmium tetroxide, uranyl

magnesium acetate, lead nitrate, and sodium citrate were obtained from Ted Pella Inc., (Redding, CA, USA).

Methods

Animals. Golden Syrian Hamsters (6–7 weeks of age) were obtained from Harlan Laboratories, Inc., (Indianapolis, IN, USA). Animals were housed in a controlled environment under a 12-h light dark cycle. Hamsters were allowed food and water ad libitum. All animal experiments were carried out under an Institutional Animal Care and Use Committee (IACUC) approved protocol. Each experiment or assay was carried out using three to six different animals per treatment groups.

Characterization of nanoparticles. Aqueous suspensions of nanoparticles were loaded on formvar coated copper grids. The primary particle size of WO_3 NPs was measured using transmission electron microscopy (TEM) (JEOL JEM-1200EX). Energy dispersive X-ray (EDX) was used to verify the elemental analysis. TEM micrographs were analyzed using ImageJ software (version 1.47a). Nanosphere™ size standards, with diameter of 102 ± 3 nm, were used as a calibration standard for measurements. Additionally, particle size analysis of suspension was also carried out by dynamic light scattering (DLS) using a Delsa Nano C Particle Size Analyzer (Beckman Coulter Inc., CA, USA). Zeta potential of the aqueous nano-suspension was measured using a Delsa Nano C Particle Size Analyzer (Beckman Coulter Inc., CA, USA) as described by Clogston *et al*.[28]

Experimental design, exposure system and aerosol. Animals were divided into three groups, a control group and two treatment groups (5 or 10 mg/m^3). For inhalation exposure study, each group was exposed for 4 h/day for four days or alternatively groups were exposed for 4 h/day for eight days to aerosolized distilled water (controls) or the respective WO_3 NPs concentrations (treated) in a whole body exposure chamber (CH Technologies Inc., NJ, USA). The time period of exposure (4 h) was selected on the basis of OECD guidelines.[29] The short-term exposure (4 days) was utilized to obtain preliminary insight to the possible deleterious effects of nano tungsten in the lungs based on other nanoparticle exposure studies.[30–32] The long-term exposure (eight days) was used to investigate the molecular mechanism of toxicity by repeated exposure of inhaled nanoparticles.

Aerosols were generated using a 6-jet collision nebulizer (BGI Inc., MA, USA) and compressed air. WO_3 NPs were suspended in sterile distilled water and sonicated prior to exposure. The suspension in the reservoir of the nebulizer was stirred continuously to ensure proper dispersion. A control unit (CH Technologies Inc., NJ, USA) was used to regulate the flow of aerosol generation air and dilution air to achieve the desired particle concentration in the chamber. Time-integrated mass aerosol concentration was measured using a gravimetric, single filter system (CH Technologies Inc., NJ, USA). Aerosol particle size distribution was monitored using a NanoScan® scanning mobility particle sizer (SMPS, TSI Inc., MN, USA). Geometric mean and geometric standard deviation of aerosol at individual exposure times were also measured. The NanoScan® SMPS was calibrated before the inhalation study with Nanosphere™ size standards, 102 ± 3 nm. Based on trials, robust protocols to maintain targeted particle concentrations for both inter- and intra-day exposure periods were developed. Additionally, the aerosol mass concentrations were verified using gravimetric analysis and *in-situ* particle agglomeration status was checked by placing a TEM grid in the chamber during optimization. To minimize incidental exposure via unintentional routes (oral/dermal), the current study follows the recommended volume of animals not to exceed by 5% of the total volume of the chamber as discussed by Wong.[33]

Bronchoalveolar lavage fluid analysis. 24-h post last exposure; hamsters were euthanized with an overdose of sodium pentobarbital. A 16-gauge catheter was inserted into the trachea and lungs were lavaged using ice-cold Dulbecco's Ca^{2+}/Mg^{2+}-free phosphate-buffered saline (DPBS). Lung lavage fluids were centrifuged (at 4°C, 800 r/min, 10 min) and the supernatant was aliquoted and stored at −80°C. The cellular fraction was resuspended in 1 mL of RPMI 1640 media and the total number of cells in bronchoalveolar lavage fluid (BALF) was determined using a Neubauer's cell counter. Microscope slide smears for differential cell count were prepared by using a cytocentrifugation and stained with PROTOCOL® HEMA 3™ staining system. Differential cell counts were carried out as described previously.[34] Prepared slide smears were also studied by dark field microscopy.

The supernatant (acellular content) was analyzed using the following biochemical assays. The total protein content was measured by the bicinchoninic acid method using Pierce BCA® Protein Assay Kit. Bovine serum albumin (BSA) was used as a protein standard. Lactate dehydrogenase (LDH) activity was measured colorimetrically using commercially available LDH Cytotoxicity Assay Kit. The assay is based on redox reactions. First, oxidation of lactate to pyruvate is catalyzed by LDH with reduction of NAD^+ to NADH. Simultaneously, diaphorase uses newly formed NADH to catalyze the reduction of the tetrazolium salt to formazan. TNF-α, a primary mediator of inflammation, was measured using TNF-α EIA Kit. The assay is an immunometric ELISA based on double-antibody ''sandwich'' technique. HRP-conjugated streptavidin was used to detect the ''sandwich.'' TNF-α was detected by measuring enzyme activity of HRP using TMB substrate. ALP activity was measured using ALP assay kit. The assay is based on the use of p-nitrophenyl phosphate (pNPP) as a phosphatase substrate that turns yellow when dephosphorylated by ALP.

Immunoblot analyses. Western blot analyses were carried out using Bio-Rad protein blotting guide protocol.[35] Immediately after lavage, lung tissues were surgically removed, rinsed with ice-cold DPBS, snap-frozen, and stored in liquid nitrogen until analyzed. Tissue homogenates were prepared using RIPA lysis buffer containing a protease inhibitor cocktail. Total protein content

was determined using Pierce BCA® Protein Assay Kit. Proteins were denatured at 70°C for 10 min, in Laemmli sample buffer containing 5% (v/v) beta-mercaptoethanol. Depending on the type of protein to be analyzed, 40–60 μg of total protein content were resolved on SDS-PAGE gels. The resolved proteins were transferred to PVDF membrane by ''wet-transfer'' method under ice-cold conditions. Blots were blocked with 5% (w/v) non-fat dry milk in Tris Buffered Saline containing Tween-20 (TBST) for 3 h at room temperature or incubated overnight at 4°C. After blocking, membranes were washed thoroughly and incubated with respective primary antibodies overnight at 4°C. All primary antibodies were prepared in rabbit and anti-rabbit IgG, HRP-linked secondary antibody (1:1000) was used to probe the membranes. The following antibody dilutions were used – cathepsin B (1:1000), TXNIP (1:500), NLRP3 (1:1000), ASC (1:1000), caspase-1 (1:1000), IL-1β (1:1000), and HMGB1 (1:1000). Anti-IgG β-actin (1:5000) was used to probe for actin that was used as a loading control. Post incubation, membranes were washed and incubated for 2 h in secondary antibody. After incubation, chemiluminescence was detected using Amersham™ ECL™ Prime Western Blotting Detection Reagent and membranes were scanned and photographed using Alfa Innotech digital imager. Obtained images were analyzed by densitometry using ImageJ software (version 1.47a). For HMGB1 protein expression, equal amount of proteins from acellular fractions of BALFs were measured as described previously.[36]

Light microscopy. Lung tissue from control and treated animals were fixed *in situ* by insufflation with 10% neutral buffered formalin (NBF) at a pressure of 20 cm of water for 2 h on ice. Following initial fixation, lungs were removed and fixed for an additional 48 h at 4°C in 10% NBF. The formalin fixed tissues were serially dehydrated using ethanol, cleared in xylene and embedded in Paraplast® X-TRA. Sections, 4–6 μm thick, were cut from tissue blocks, mounted on glass slides, and stained with hematoxylin and eosin. Dark field microscopy was also carried out using dark field condenser (CytoViva Inc., Auburn, AL, USA) and an oil immersion objective (Olympus America Inc., Hauppauge, NY, USA), attached to Olympus BH-2 microscope (Olympus America Inc., Hauppauge, NY, USA) with a digital camera system.

Electron microscopy. Changes in morphology at the ultrastructural level associated with nanoparticle exposure to the cells and tissues were examined by scanning and transmission electron microscope. For TEM, animals were euthanized as above, and lungs were fixed *in situ* by insufflation with 3% glutaraldehyde in 0.1 M sodium cacodylate buffer at a pressure of 20 cm of water for 1 h. Collected cells from BALFs were fixed in 3% glutaraldehyde in 0.1 M sodium cacodylate buffer for 1 hr. Following initial fixation, both tissue blocks and cells recovered from BALF were washed in 0.1 M sodium cacodylate buffer and post-fixed in 1% osmium tetroxide for 2 h. Samples were stained *en bloc* with 1% uranyl magnesium acetate overnight, serially dehydrated in acetone and infiltrated in sequentially increasing concentration of LX112-Araldite mixture to 100% and embedded in pure LX112-Araldite mixture. Tissue blocks were sectioned (70–100 nm), collected on 300 mesh copper grids, and stained with uranyl acetate and lead citrate. All specimens were examined using a JEOL JEM-1200EX TEM at accelerating voltage of 80 kV.

For scanning electron microscope (SEM), BALF cells were seeded on 12 mm glass coverslips in a 24-well plate using RPMI 1640 media supplemented with 10% fetal bovine serum (FBS). Cells were allowed to incubate at 37°C in humidified atmosphere of 5% CO_2 for 4–6 h. Cells were washed with DPBS and fixed with 2.5% glutaraldehyde in 0.1 M sodium cacodylate buffer. Fixed lung tissue, described previously, was also used for morphological analysis using SEM. Samples were washed thoroughly with 0.1 M sodium cacodylate buffer after fixation. Specimens were then serially dehydrated to 100% acetone and dried using the critical point method. Samples were coated with platinum/palladium and were examined using an SEM (JEOL JSM 6010LA).

Statistical analysis. Unless otherwise indicated, data were presented as the mean ± SEM. Statistical analysis was carried out using Graph Pad Prism® Version 5.0 (San Diego, CA, USA) with significance tested among and between groups using one-way analysis of variance (ANOVA) followed by Neumann Keuls multiple comparisons *post hoc* analysis. Differences between treatment groups were considered to be significant at the 95% level ($P < 0.05$) and noted based on following hierarchy $^{*}P < 0.05$, $^{**}P < 0.01$, $^{***}P < 0.001$.

Results

Nanoparticle characterization

WO_3 NPs were characterized by using TEM (Figure 1(a)) and DLS (Figure 1(b)). Randomly selected TEM micrographs were analyzed for WO_3 NPs particle size determination with an average number of 150 individual nanoparticles. As observed by TEM, the nanoparticles were approximately spherical in shape and were well dispersed with an average external diameter of 71 ± 34 nm. Student's t-test was carried out to compare means of measurements from individual micrographs, $t(5) = 1.744$, $P = 0.1561$. The hydrodynamic diameter, as measured using DLS, was found to be 157 ± 56 nm. Despite sonication, agglomerates were also observed along with individual nanoparticles. Nanosphere™ size standards with a diameter of 102 ± 3 nm were used as internal control to validate the measurements.

Analysis of the BALF

Hamsters were exposed to low (5 mg/m^3) or high (10 mg/m^3) concentrations of WO_3 NPs for 4 h/day for four consecutive days to assess possible lung injury and cellular changes caused by particle exposure.

A short-term inhalation exposure to WO_3 NPs resulted in significant increase ($P < 0.05$) in total cells in the BALF. Cell numbers were increased from $15.6 \pm 0.58 \times 10^4$ cells/ml

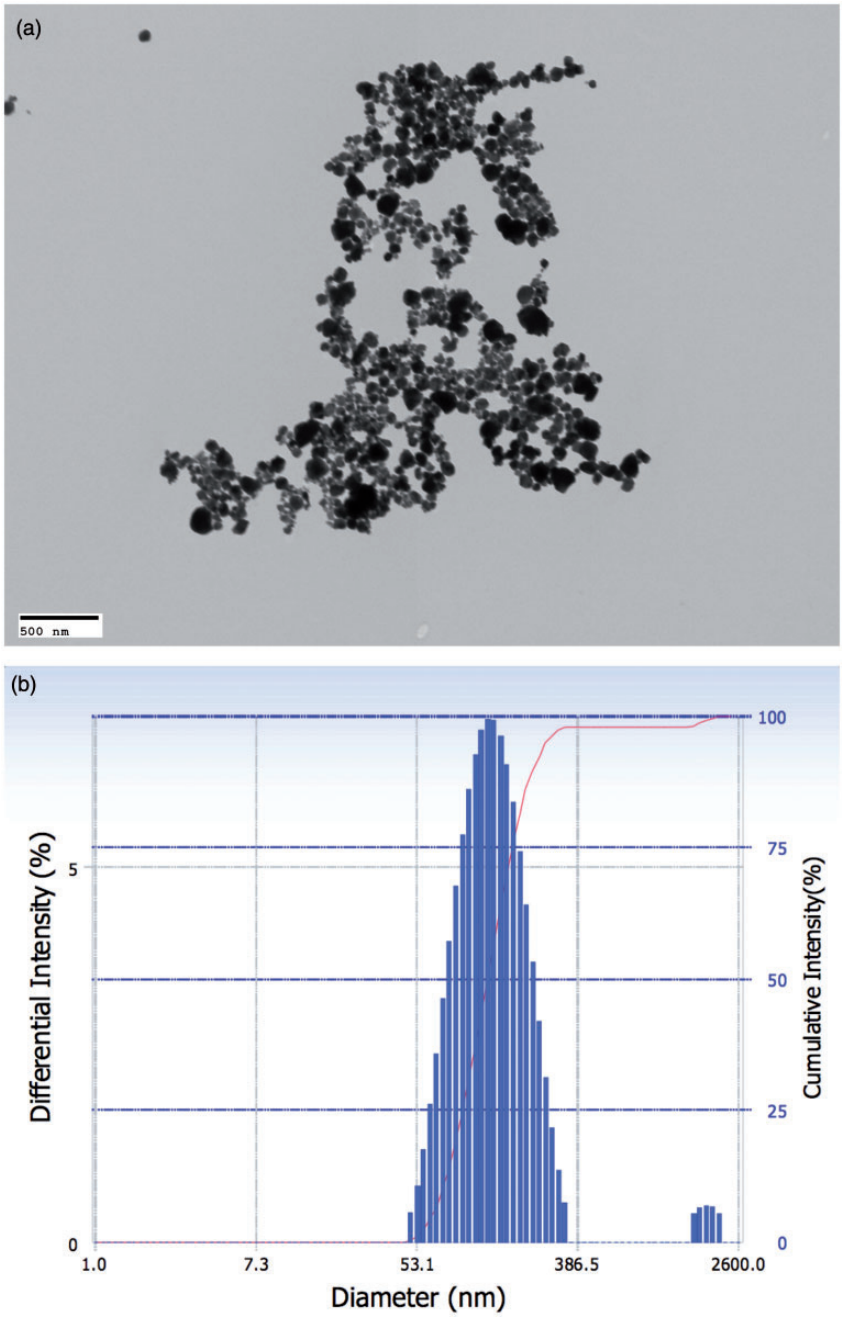

Figure 1 WO_3 NPs were characterized by TEM and DLS. (a) Representative electron micrograph obtained for aqueous suspension of WO_3 NPs on formvar-coated copper grids and examined using a TEM. The average external diameter of WO_3 NPs was determined to be 71 ± 34 nm (Scale bar represents 500 nm). (b) Representative distribution of particle size in aqueous suspension of WO_3 NPs measured using DLS. The average hydrodynamic diameter was determined to be 157 ± 56 nm. (A color version of this figure is available in the online journal.)

in the controls to $22.4 \pm 0.06 \times 10^4$ cells/ml and $23.9 \pm 2.56 \times 10^4$ cells/ml for treated groups (5 and 10 mg/m^3 respectively), Figure 2(a). Inhalation of WO_3 NPs led to an increase in neutrophils from $0.08 \pm 0.06 \times 10^4$ cells/ml in controls to $2.3 \pm 0.6 \times 10^4$ cells/ml in the 5 mg/m^3 or to $9.3 \pm 3.3 \times 10^4$ cells/ml in the 10 mg/m^3 groups treated with WO_3 NPs, Figure 2(c). Only the increases in the 10 mg/m^3 WO_3 NPs-treated groups were significant, $P < 0.05$. Lymphocytes numbers were also increased in the BALF of treated animals as compared to controls. The number of lymphocytes in the BALF of treated animals was 3.2 fold higher for the 5 mg/m^3 of WO_3 NPs-treated group and 2-fold increase in 10 mg/m^3 of WO_3 NPs-treated group as compared to controls. Only the former increases were significant ($P < 0.05$), Figure 2(c). Pulmonary macrophages were increased in numbers in nanoparticle-treated groups, but such increases were not significantly different from controls, Figure 2(c).

Markers of inflammation were assessed in the BALF, Figure 3. Inhalation exposure of hamsters to 10 mg/m^3

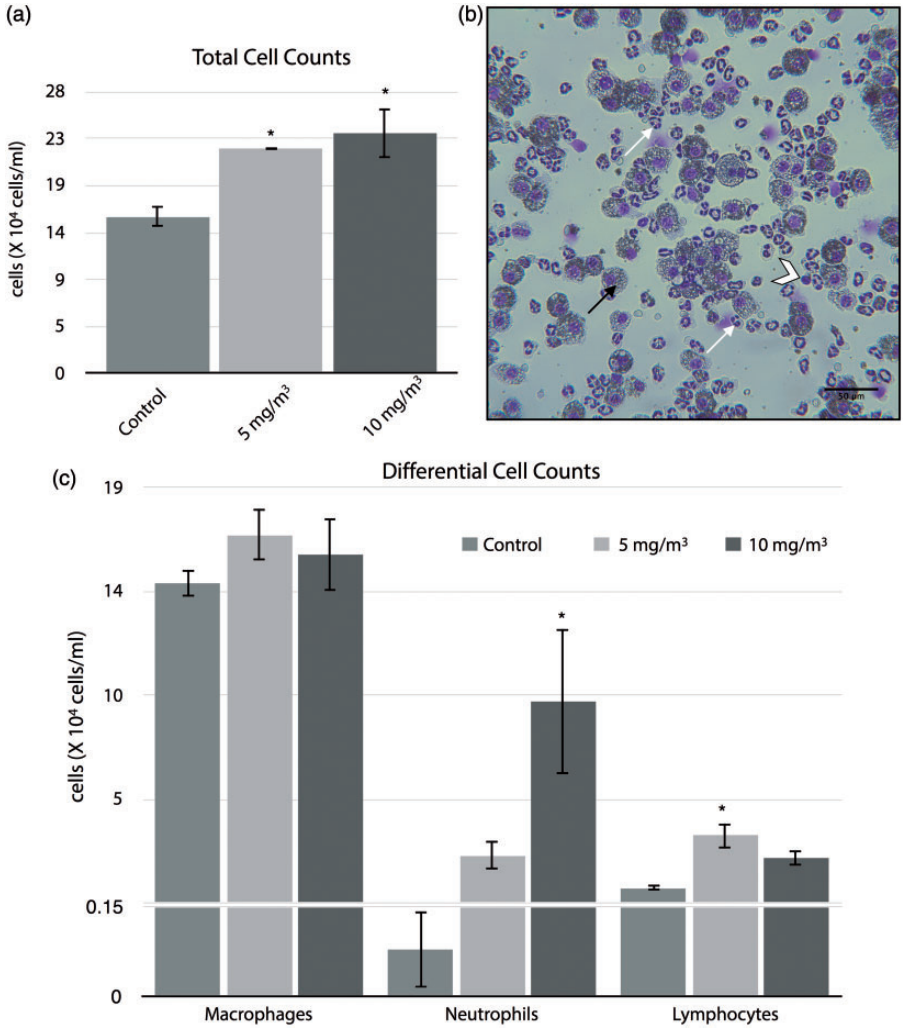

Figure 2 Figure representing the concentration-response effect to WO_3 NPs of markers for inflammation and cytotoxicity in the bronchoalveolar lavage collected from hamster lungs, 24 h post-inhalation. BAL fluids and cell were separated by centrifugation. The cells were re-suspended in 1 mL of RPMI 1640 media, followed by determination of total cell numbers (a) by direct counting with the use of a hemocytometer. The total cell numbers were significantly ($P < 0.05$) increased ~1.5 folds in the treatment groups. (b) Photomicrograph of BALF cells from lung exposed to 10 mg/m^3 of WO_3 NPs for 4 h/day for four days. Note the presence of PMNs (arrow), lymphocyte (chevron), and macrophages (dark arrow). Differential counts (c), slide smears were prepared by using a cytocentrifuge showed neutrophilia by a statistically significant ($P < 0.05$), 27% increase in neutrophils (10 mg/m^3 treated group) as compared to control. (A color version of this figure is available in the online journal.)

WO_3 NPs induced a 1.7-fold increase when compared to controls in total protein content of the BALF, Figure 3(a). A 1.8-fold increase in LDH activity as compared to controls was seen in the BALF of 10 mg/m^3 WO_3 NPs-treated animals, Figure 3(b). The ALP (Figure 3(c)) activity was significantly increased in the BALF of hamsters exposed to 5 mg/m^3 ($P < 0.05$) or 10 mg/m^3 ($P < 0.01$) concentrations of WO_3 NPs when compared to controls. ALP activity of the lavage fluids was 90.3 ± 2.9 U/L or 92.5 ± 2.5 U/L ($P < 0.01$), respectively, for the treated groups and the control group was 76.4 ± 2 U/L. The levels of pro-inflammatory cytokine, TNF-α, released into the BALF was significantly ($P < 0.05$) increased in the 10 mg/m^3 treated group (2-fold compared to controls), Figure 3(d). Statistically significant ($P < 0.05$), concentration-dependent increases in HMGB1 protein in both treatment groups were observed (1.5 and 2.9-fold change in 5 and 10 mg/m^3 groups, respectively) when compared to controls, Figure 3(e).

Morphologic analysis of the lung parenchyma

Histopathological examination of lung tissue revealed the deposition of WO_3 NPs in the bronchi, bronchioles, alveoli, and the alveolar interstitium of lung parenchyma in both treatment groups, Figure 4. Control animals, treated with aerosolized water, exhibited no signs of structural abnormalities, Figure 4(a), while lung sections from treated animals indicated the presence of hyperplasia as seen in Figure 4(b). Dark field photomicrograph of treated lung tissue had deposits of WO_3 NPs in lung epithelium and nanoparticle laden macrophages in the bronchiolar lumen, Figure 4(c). Dark field photomicrographs, Figure 4(d), of BALF cyto-smears from control animals lacked the birefringence particles that were seen in treated specimens. Photomicrographs of cyto-smears of BALF cells, treated with WO_3 NPs at either 5 mg/m^3, Figure 4(e) or 10 mg/m^3, Figure 4(f), concentrations indicate the presence of WO_3 NPs in pulmonary macrophages.

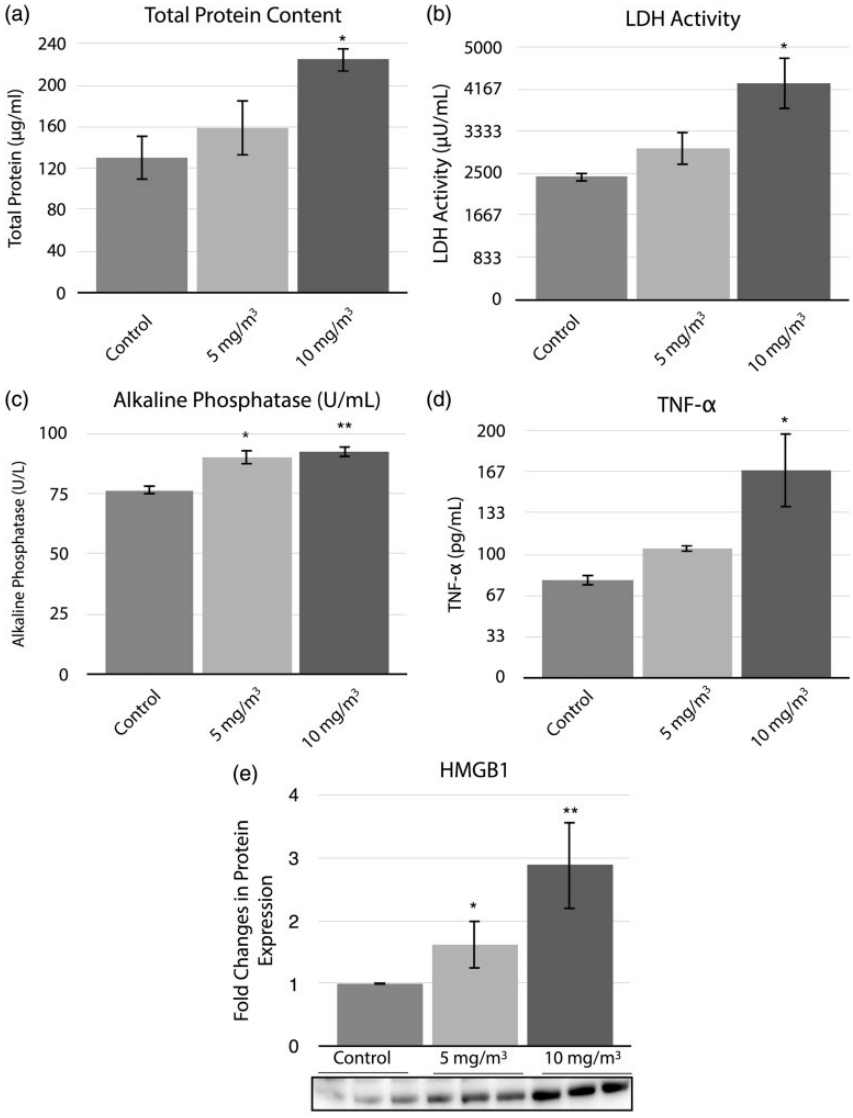

Figure 3 Histograms representing total protein content (a), LDH activity (b), ALP activity (c), levels of TNF-α (d) and HMGB1(e) protein expression. The parameters from acellular fractions of BALF were assayed as described in methods section. Total protein content and LDH activity of the acellular fractions showed a significant ($P < 0.05$) 1.7 and 1.8 fold increase, respectively, in 10 mg/m^3 treated group when compared to control. Alkaline phosphatase activity was significantly ($P < 0.05$ and $P < 0.01$) different in both the treatment groups from controls. (d) The levels of TNF-α were significantly ($P < 0.05$) increased by two folds in the animals treated with 10 mg/m^3 of WO_3 NPs. Equal amount of protein from acellular fractions of BALFs from controls and treated animals examined by Western blot analyses showed a significant increase (nearly three-fold in 10 mg/m^3 treated animals) in HMGB1 protein. (e) The histogram represents the changes in protein expression

Scanning electron microscopy was used to assess the morphological changes associated with exposure of WO_3 NPs in isolated pulmonary macrophages and lung tissues. Macrophages from control animals have a ruffled surface, typical of phagocytes and were otherwise unremarkable, Figure 5(a). Scanning electron micrographs, Figure 5(b), of macrophages recovered from BALF of exposed animals revealed the presence of cell membrane blebs, an indication of cell swelling, and presence of the fluid filled sacs. Control animals, treated with aerosolized water, showed no sign of alteration to the lung airway epithelial linings with intact intracellular tight junctions between cells, Figure 5(c). The surface of epithelial cells from the airways of control animals was flat and covered with cilia. Photomicrographs of the epithelial linings of airways from the lung tissue of animals exposed to WO_3 NPs were domed showing signs of the formation of membrane blebs, Figure 5(d), with what appears to be a reduction in the number of cilia present. SEM images of alveolar surfaces from controls lacked WO_3 NPs and had an unremarkable appearance, Figure 5(e). Photomicrographs of alveolar surfaces from treated animals show a granular deposition of WO_3 NPs on the alveolar epithelium as seen in Figure 5(f).

TEM was utilized to investigate the deposition pattern of WO_3 NPs post-inhalation in the parenchyma of the lung. Figure 6(a) is an electron micrograph of a portion of an alveolar septum from a vehicle-treated control. Cellular organelles such as lamellar bodies in type II pneumocytes have normal appearance of lamellae within a membrane bound vesicle. The alveolar surface was

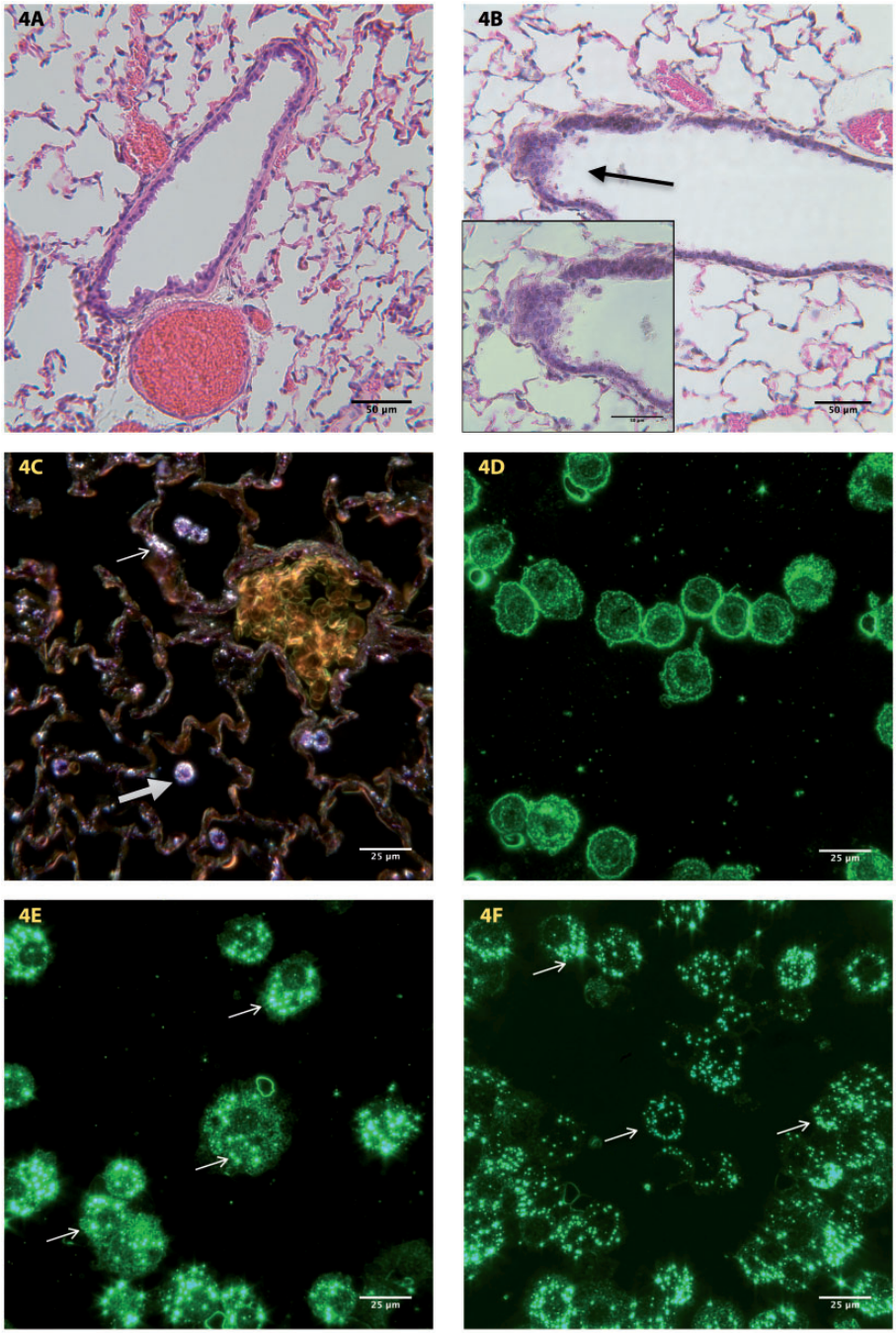

Figure 4 Representative photomicrographs of formalin fixed tissue section from the lungs of (a) control and (b) animals treated with a concentration 10 mg/m^3 of WO_3 NPs. H&E stained sections of treated animals showed areas of hyperplasia (arrow). The inset shows a higher magnification of the arrowed region. (c) Sections from lungs of treated animals examined by dark field microscopy reveal the presence of WO_3 NPs within the epithelium (arrow) and in macrophages (open arrows). (d) Dark field micrographs of BALF cyto-smears from control animals prepared as described in methods section, lacked the birefringence particles that were seen (arrow) in macrophages from animals treated with 5 mg/m^3 (e) and 10 mg/m^3 (f) of WO_3 NPs. (A color version of this figure is available in the online journal.)

covered by type I pneumocyte with interspersed type II cells surrounding interstitial cells (IS). Figure 6(b) is a micrograph of an alveolar septum from the lung of a hamster treated by inhalation with 10 mg/m^3 WO_3 NPs. The micrograph shows the presence of nanoparticles in macrophages, type I, and type II pneumocytes. Examination of the macrophages by TEM from the lungs of animals treated with 10 mg/m^3 WO_3 NPs, Figure 6(c) and (d), indicates the presence of nanoparticles within phagosomes, while Figure 6(d) is an enlargement of an area from Figure 6(c) that shows WO_3 NPs in the form of agglomerates, aggregates, and individual particles. Membrane blebbings were also seen as shown in Figure 6(c) and (d). Such are consistent with the SEM histopathological evaluation. Spectral output from TEM micrograph was analyzed using EDX analysis. By focusing the electron beam on nanoparticles,

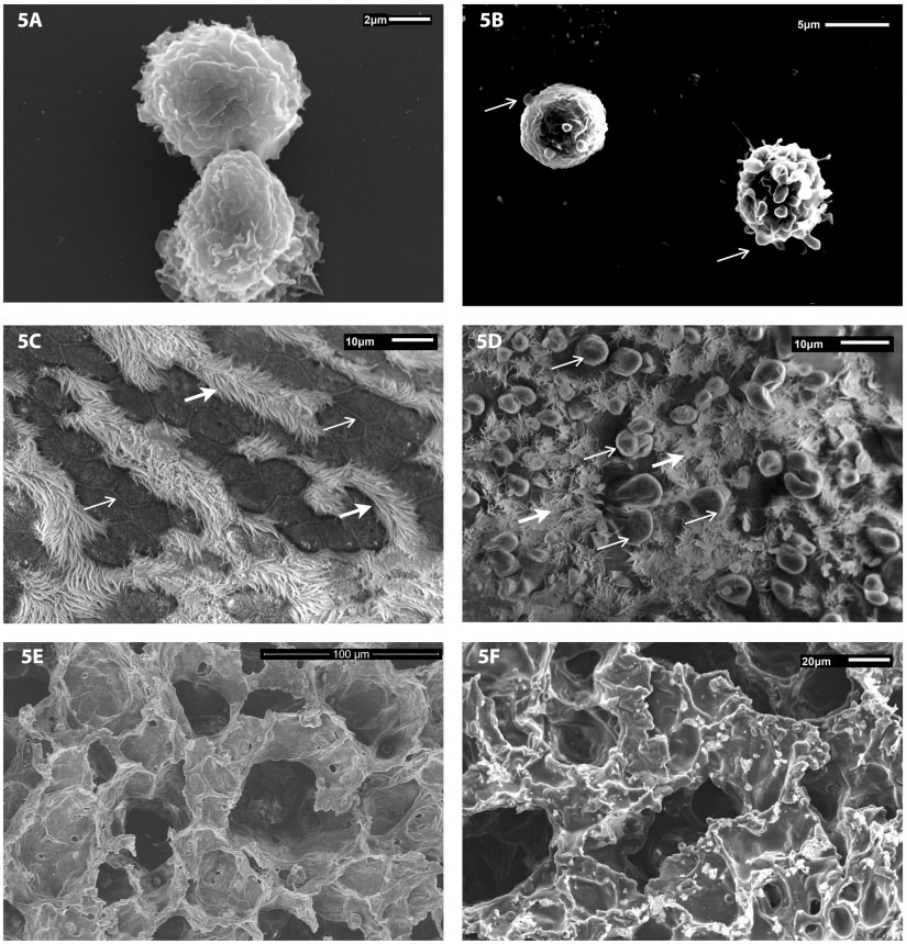

Figure 5 Representative scanning electron micrographs of pulmonary macrophages isolated from BALF of animals exposed by inhalation to a concentration of 10 mg/m^3 of WO_3 NPs. Cellular fractions of BALF were seeded on coverslips with RPMI 1640 media. SEM photomicrographs of lung tissue from control and treated animals were fixed in 3% glutaraldehyde and processed as described in methods. (a) Macrophages from control animals had a ruffled surface, typical of phagocytes while those from WO_3 NPs exposed animals' (b) had surface membrane blebs (arrow) that are a characteristic feature of apoptosis. (c) The surface of airways from control animals had no sign of membrane damage, with rows of cilia (open arrow) and intercellular tight junctions clearly visible (arrow). (d) In contrast, the luminal surface of airway epithelia of hamsters treated with 10 mg/m^3 of WO_3 NPs displayed numerous membrane blebs (arrows) with interspersed cilia (open arrow). (e) SEM images of alveolar surfaces from controls lacked WO_3 NPs and had an unremarkable appearance. (f) Photomicrographs of alveolar surfaces show a granular deposition of WO_3 NPs

it was possible to confirm the deposition of WO_3 NPs within macrophage Figure 6(e). The deposition of WO_3 NPs was also noted in the airway epithelium (Figure 6(f)), which had numerous membrane blebs on their surface.

The role of the inflammasome

Animals were exposed to low (5 mg/m^3) and high (10 mg/m^3) concentrations of WO_3 NPs for 4 h/day for eight consecutive days to study the role of inflammasomes. The cathepsin family of proenzymes is one of the proteolytic proteins that has been implicated in the activation of the inflammasomes. Changes in cathepsin B expression in the lungs of WO_3 NPs-treated animals were assessed, Figure 7(a). There was a significant ($P < 0.05$) increase in cathepsin B protein in both the treatment groups (1.28 and 1.26 fold changes in relative protein expression for 5 and 10 mg/m^3, respectively). WO_3 NPs-mediated activation of NLRP3 was investigated by immunoblot analyses of the protein expression of TXNIP. Upon exposure to WO_3 NPs, a statistically significant ($P < 0.05$) increases in TXNIP protein expression, 2.85 and 3.38-fold, were seen in the 5 and 10 mg/m^3 treatment groups compared to the control Figure 7(b). Activation of NLRP3 leads to the assembly and activation of the NLRP3 inflammasome. Immunoblot analyses of NLRP3, ASC, Caspase-1, and IL-1β indicated the formation of the active inflammasome following WO_3 NP exposure. Expressions of NLRP3, Figure 7(c), were significantly increased, $P < 0.05$ or $P < 0.01$, by 1.5 fold or 1.7 fold, above control in animals treated with 5 mg/m^3 or 10 mg/m^3, respectively. The levels of ASC were significantly increased $P < 0.05$ by 2 fold in lungs of animals treated with 10 mg/m^3 WO_3 NPs as compared to control's, Figure 7(d). WO_3 NPs exposure led to a significant increase ($P < 0.05$) by 2.32 fold in activated caspase-1 in 10 mg/m^3 treated animals when compared to controls, Figure 7(e). The presence of activated caspase-1 indicates its cleavage by the NLRP3 inflammasome assembly. In addition, it was observed that there was a significant increase

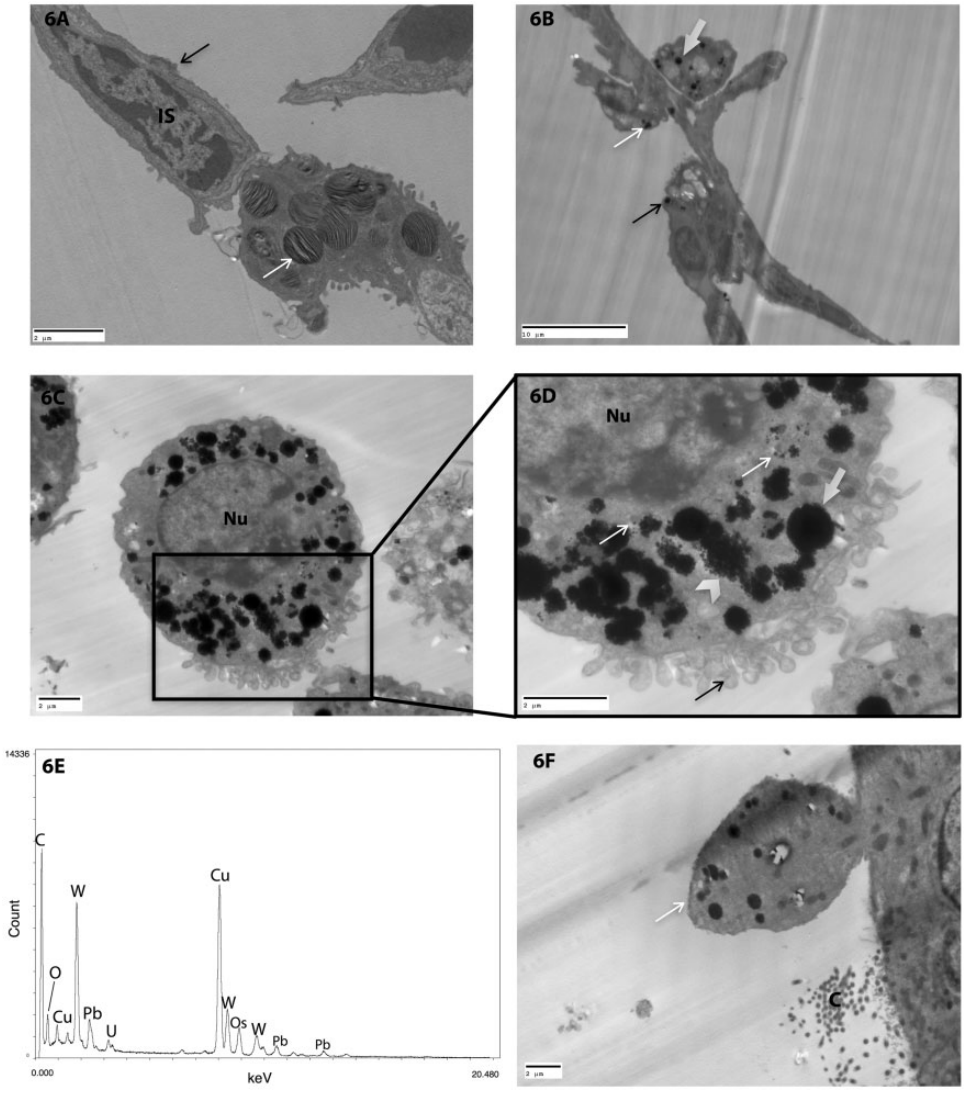

Figure 6 Representative TEM photomicrographs of lung tissue taken from control and treated animals fixed in 3% glutaraldehyde and processed as described in methods. (a) The micrograph is of a portion of an alveolar septum from a vehicle-treated control. Note the presence of typical lamellar bodies (arrow) in type II pneumocytes and the alveolar surface covered with type I pneumocyte (dark arrow) surrounding interstitial cells (IS). (b) Alveolar septum from the lung of a hamster treated by inhalation with 10 mg/m^3 WO_3 NPs shows uptake of nanoparticles in macrophages (open arrow), type I (arrow) and type II pneumocytes (dark arrow). (c) Micrograph of a WO_3 NPs laden macrophage (nucleus marked Nu) from the lung of a treated animal, (d) an enlarged area from Figure (c) showing metal particles as agglomerates (open arrows), aggregates (chevron), and individual particles (arrows). Note also the presence of membrane blebs at the cell's surface (dark arrow). (e) Spectral output from thin section analyzed using energy dispersive X-ray analysis (EDX) of pulmonary macrophage animal treated with 10 mg/m^3 WO_3 NPs confirms the elemental nature of nanoparticles. (f) Electron micrograph of the surface of an airway epithelial cell from a treated animal. A large surface bleb (arrow) that contain numerous vesicles filled with WO_3 NPs, cross sections of cilia (marked C) can be seen on the cell's surface confirming the presence of bleb in the airway epithelium

($P < 0.05$ or $P < 0.01$) by a 1.67 fold or 2.26 fold, in IL-1β in the lung parenchyma of the 5 mg/m^3 or 10 mg/m^3 treated groups respectively when compared to control group, Figure 7(f). Such an increase in IL-1β production can be attributed to active caspase-1 that is in turn, activated by the NLRP3 inflammasome.

Discussion

WO_3 NPs were used to cause perturbations in the lungs of Golden Syrian Hamsters in order to study their role in the production of lung injury, in the activation of inflammasomes, and in the induction of pyroptosis. Activation of inflammasomes with concomitant release of IL-1β is at the core of pulmonary inflammation[37,38] and tissue destruction that may subsequently lead to pulmonary fibrosis.[39–41] Until recently, tungsten and its related compounds were considered relatively inert toxicologically. Such belief was supported by a study[42] that found intra-tracheal instillation of pure tungsten particles 1–5 μm in size did not cause significant changes in inflammatory markers or lead to apparent pulmonary toxicity. However, the toxic potential of tungsten and its compounds may be attributed more to their physical characteristics than to their elemental nature. Several properties of nanoparticles, such as size, shape, morphology as well as composition, play a major role in their toxicity.[43] Among these properties, the size

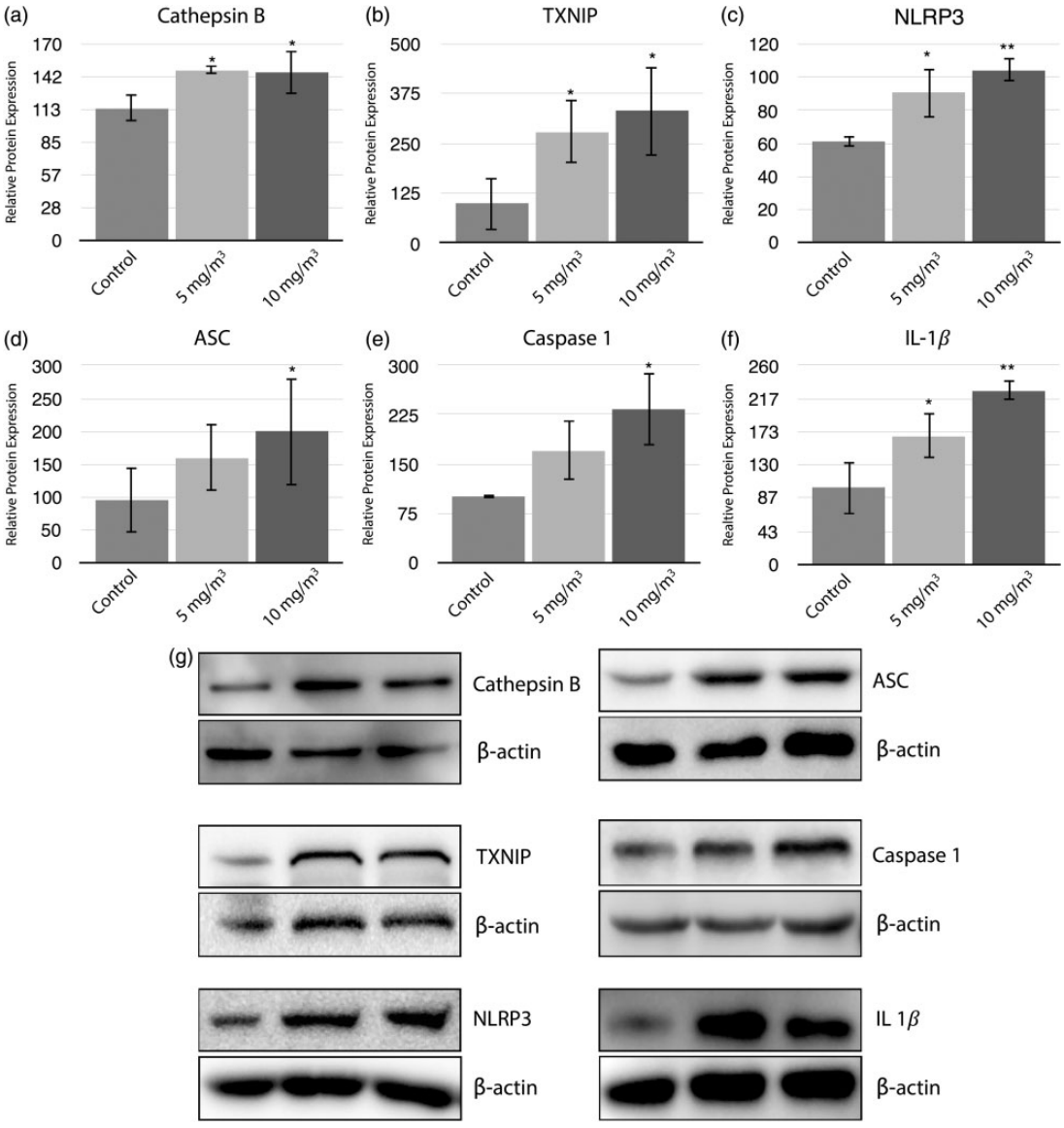

Figure 7 Histograms (a–f) represent a densitometric analysis of immunoblot for detection and quantitation of components and associated proteins of the inflammasome pathway. Proteins were analyzed using immunoblot analysis as described in methods section. Relative protein expressions showed 1.26, 3.38, 1.7, 2.09, 2.32, and 2.26 fold increase in cathepsin B (a), TXNIP (b), NLRP3 (c), ASC (d), Caspase-1 (e), and IL-1β (f), respectively, for animal treated with 10 mg/m^3 WO_3 NPs. (g) Representative immunoblots for respective proteins normalized to β-actin

of the particle has a pivotal role. WO_3 NPs were characterized before their use by DLS and by TEM. The elemental composition of these particles was confirmed by TEM using EDX analysis. Prior to analyses or initiation of animal exposure, particle suspensions were sonicated. A previous study[44] has reported that sonication of nano-suspensions reduces agglomeration of particles with minimal effects on their surface charges. The zeta potential of the WO_3 NPs used in this work was determined to be -46.9 ± 3.8 mV indicating a stable nanoparticle suspension.[45] The size differences between the two procedures (DLS and TEM) are related in part to ''wet phase'' versus ''dry phase'' analyses as described previously.[44] The ''wet phase'' being aqueous suspensions of nanoparticles measured by DLS and ''dry phase'' being samples measured by TEM. Such size differences in nanoparticles were also seen with a variety of materials such as carbon nanotubes, silver, titanium dioxide, aluminum oxides, copper and silicon dioxide nanoparticles and also with carbon black.[45]

Aerosol characteristics were monitored continuously for particle size, distribution, and mass concentration using a NanoScan® SMPS. Aerosol characterization using SMPS indicated an average geometric mean particle diameter of 202 ± 49 nm within the exposure chamber. Such an increase in size may be attributed to aggregation and/or agglomeration of nanoparticles, perhaps within the chamber. In addition, these finding also help to explain the increased particle size seen with DLS measurements, when compared to the TEM determinations. *In-situ* aggregation and agglomeration status of nanoparticles were checked by TEM. WO_3 NPs deposited on TEM grids set in the inhalation chamber (*in-situ)* revealed aggregates, and agglomerates as well

as individual particles. Such findings further support the theory that agglomeration of particles occurs within the chamber. Under the conditions used particle agglomerations are unavoidable and are also comparable to those seen in other studies.[41,46,47] In addition to the intended inhalation route, animals may receive an incidental exposure of nanoparticle primarily via oral route due to grooming behavior. A study[48] found that the intake of nanoparticles occur on oral exposure of WO_3 NPs, most of which are excreted via feces. Following such exposure, the bio-distribution of some of the tungsten particles transferred across the gut were reported to be highest in the liver leading to genotoxicity, in the bone marrow and peripheral blood cells. In the current study, WO_3 NPs deposited on the internal surface of the chamber were detected by examination of formvar-coated copper grids placed in the chamber. The number of particles deposited on the surface of these grids was extremely low. As a result of this small deposition, it is unlikely that the particulate tungsten delivered via a self-grooming route would have significantly altered the pulmonary exposure levels of nanoparticle as reported by other study[49] using similar methodology.

Golden Syrian Hamsters were used as an animal model as they have a low occurrence of pulmonary infections and spontaneous lung tumors.[50] This animal model has also been used to study acute and chronic disorders such as pulmonary fibrosis,[51,52] emphysema,[53] acute lung injury,[54] and pneumonia.[55,56] Such studies have provided useful data for comparison to human diseases and represents a suitable model for the study of pulmonary response to nanomaterials. In addition, inbred strains of mice and rats have been noted to have different, strain-dependent susceptibility to inhaled materials such as cigarette smoke[57] and nanomaterial such as Quantum Dots.[58] These strain differences appear to contribute to altered biological responses that may yield conflicting data. Golden Syrian hamsters, an outbred animal used in this study, are not known to have such strain differences. Further, the hamster model is also considered a better *in-vivo* model for lung inflammation and activation of neutrophils as described by Corteling *et al*.[59]

The increases in total leukocyte numbers (Figure 2(a)) along with neutrophil influx (Figure 2(c)) indicate the induction of pulmonary inflammatory response to WO_3 NPs as demonstrated by other nanomaterials.[46,60] Normally, tight junctions formed by epithelial and endothelial cells prevent the loss of protein from the vasculature.[61] Increased levels of protein within the BALF (Figure 3(a)) suggest a breakdown of epithelial/endothelial barrier function that is also associated with inflammation and cell injury. LDH activity increase seen in the BALF of exposed animals (Figure 3(b)) is a hallmark of cellular damage and is often used as a primary indicator of cell injury as its release is indicative of loss of membrane integrity.[30,62] Such findings are consistent with those of other studies[42,46,63–65] of animals exposed to different materials such as titanium dioxide, airborne fine particulate matter, cerium oxide, and metal tungsten alloys in nanoparticle form. Elevated ALP (Figure 3(c)) activity in the BALF of treated hamsters as compared to controls is a marker of type II pneumocyte injury[66] and an increase of this enzyme is a further indicator of damage to the alveolar epithelium. In addition, to markers of injury, perturbation of pulmonary cells often stimulates the release of cytokines that are associated with an inflammatory response.[67] The increases in pro-inflammatory cytokines, TNF-α (Figure 3(d)), and IL-1β (Figure 7(f)), seen in WO_3 NPs-treated hamsters play a significant role in pulmonary inflammation.

The presence of nanoparticles, seen in dark field micrographs (Figure 4(c), (e) and (f)), in the lung parenchyma, and in macrophage of treated animals indicates that inhaled WO_3 NPs can be inspired deep into the lung parenchyma and reach alveolar surfaces. The morphological study utilizing SEM (Figure 5) exhibited changes in airway epithelial surfaces consistent with cell injury (Figure 5). Alveolar macrophages play a pivotal role in clearing inhaled particulate matter and the removal of cellular debris from the alveolar surfaces by phagocytosis. WO_3 NPs were seen in macrophages in tissue sections from the lung of nanoparticle-exposed hamsters using light and electron microscopy. TEM examination of alveolar macrophages from treated animals indicated the presence of particles, primarily as agglomerates, in the phagolysosomes of macrophages (Figure 6(c) and (d)). Aggregates, agglomerates, and individual particles were also seen in alveolar epithelial cells (Figure 6). The distribution of such WO_3 NPs was primarily in membrane bound vesicles in pneumocytes. Intracellular nanoparticle accumulation in lung epithelial cells has been previously noted in animals exposed to multi-walled carbon nanotubes.[37] Such findings suggest that these materials were taken into the cells by phagocytosis. Phagocytosis has been clearly indicated as a function of type II pneumocytes,[68] while it has not been shown in type I pneumocytes. The distribution of WO_3 NPs seen in this study was similar to that of different nanomaterials reported in other investigations.[37,69,70] In contrast, Yazdi *et al*.[21] reported TiO_2 nanoparticles as free in the cytoplasm of cells.

The NLR family pyrin domain-containing protein 3 (NLRP3) inflammasome is a large cytosolic multi-protein complex that assembles in response to a variety of stimuli. The oligomerization of the NLRP3 inflammasomes and its components was studied by Western blot analyses (Figure 7). The data from these experiments support the potential activation of the inflammasomes in WO_3 NPs exposed lung tissue. Various studies have shown the activation of the NLRP3 inflammasome by titanium dioxide, silicon dioxide, zinc oxide in the form of nanoparticles, and by amino-functionalized polystyrene nanoparticles, multi-walled carbon nanotubes, and cigarette smoke.[21,26,38,41] In the current study, a statistically significant increase in cathepsin B (Figure 7(a)) in hamster lungs exposed to WO_3 NPs suggests activation of inflammasome as shown by nanomaterials composed of silica crystals.[22] In addition, the release of cathepsin B is known to induce mitochondrial dysfunction[71] that is associated with the formation of inflammasomes. The release of cathepsin B has been shown to be induced by other materials in nano-form such as titanium dioxide, zinc oxide, silicon dioxide.[21] Immunoblot analyses of lung tissue extracts from hamster

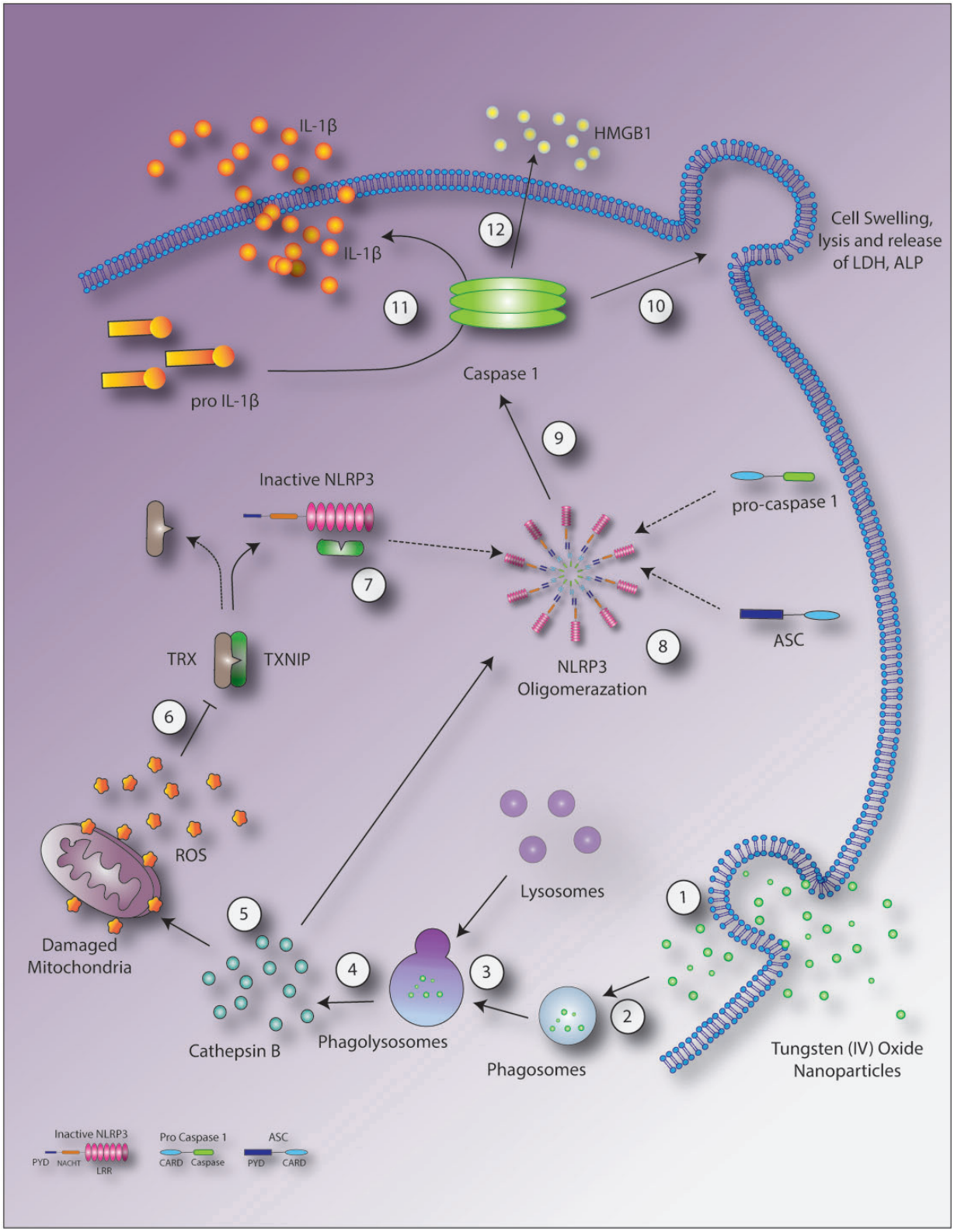

Figure 8 Schematic representation of proposed mechanisms mediated by WO_3 NPs. WO_3 NPs enter into cell (1) through the membrane or in the form of a phagosome (2), resulting in lysosomal fusion (3) with phagolysosome causing disruption and cytoplasmic release of cathepsin B (4). Alternatively, the free particles in cytoplasm may directly interact with cellular components such as mitochondria leading to oxidative stress. Cathepsin B mediates direct NLRP3 oligomerization or ROS formation via mitochondrial membrane disruption (5). ROS in turn facilitates the dissociation of TXNIP from its inhibitor TRX (6). Newly dissociated TXNIP, binds to inactive NLRP3 (7) resulting in NLRP3 activation and subsequent oligomerization (8) which activates caspase-1 (9). Active caspase-1 mediates cell swelling and lysis (10), the cleavage of pro-IL-1β to IL-1β (11) and the release of HMGB1 (12). (A color version of this figure is available in the online journal.)

exposed to WO_3 NPs indicated a significant ($P < 0.05$) increase in TXNIP (Figure 7(b)) indicating production of ROS. Nanomaterials composed of silica, titanium dioxide, or tungsten carbide-cobalt[72–74] suggest the production of ROS induced by these materials leads to oxidative stress and cell death. Further, *in vitro* data[75] show the generation of ROS in cultured rat pleural mesothelial cells when they were treated with WO_3 NPs.

The inflammasome activation of caspase-1 also regulates the release of alarmins such as HMGB1.[76] Increase in HMGB1 levels suggests the role of inflammasome as studied by Lamkanfi *et al*.[76] indicating that HMGB1 secretion from LPS-primed macrophages requires inflammasome components, and caspase-1 activation occurs downstream of inflammasome assembly. Also, the increase in HMBG1 may be an indication of macrophage activation.[77] The oligomerised assembly of NLRP3 leads to the activation of caspase-1 that then leads to the secretion of the pro-inflammatory cytokine, IL-1β and IL-18.[20,27,78] Such an increase in IL-1β was significant in lung tissues of hamsters treated with WO_3 NPs. Vanwinkle *et al*.[79] have shown nanoparticle uptake by type I alveolar epithelial cells that leads to oxidative stress. Such data support the findings of the current study that indicate uptake of WO_3 NPs by pulmonary epithelial cells resulting in the activation of NLRP3. The data from this study indicates WO_3 NPs-induced oligomerization of the NLRP3 inflammasome and associated release of HMGB1 and IL-1β.

In summary (Figure 8), the toxic potential of inhaled WO_3 NPs in the lung was investigated. Cellular location of WO_3 NPs and agglomeration pattern of particles in alveolar macrophages and lung epithelial cells on inhalation exposure was confirmed using microscopy. Deposition of particles in alveolar macrophages and epithelial linings may, in turn, be responsible for induction of inflammation. Results of biochemical analysis of BALF indicated the induction of pro-inflammatory cytokines that may lead to an increase in microvascular permeability and cellular damage to lung epithelium. Such data suggest a molecular mechanism for activation of inflammasome that propagates the inflammatory response via caspase-1. Upon inhalation of WO_3 NPs, these particles were phagocytized by macrophages along with their entry into the epithelial tissues. Data from this study suggest three primary signaling mechanisms, leading to activation of the NLRP3 inflammasomes and cytotoxicity – lysosomal destabilization resulting in the release of cathepsin B, nanoparticles directly or via released cathepsin B disrupting mitochondrial membranes, with associated ROS generation that may cause NLRP3 activation and caspase-1-dependent release of HMGB1. Such conclusions are supported by knock-out models of inflammasome activation[76] and direct proportionality of the generation of ROS to the activation of inflammasomes.[80]

Authors' contributions: MVP carried out all the experiments. MVP, OOA, and JMC designed the experiments and analyzed data. MVP and JMC wrote the manuscript. BMM assisted in scanning electron microscopy. All authors contributed to editing and reviewing of the manuscript.

ACKNOWLEDGEMENTS

The research was funded by St. John's University, Queens, NY.

DECLARATION OF CONFLICTING INTERESTS

The author(s) declared no potential conflicts of interest with respect to the research, authorship, and/or publication of this article.

REFERENCES

1. Kerley CR, Easterly CE, Eckerman KF. *Environmental acceptability of high-performance alternatives for depleted uranium penetrators*. Oak Ridge, TN: Oak Ridge National Laboratory, 1996
2. Stanley Lillie MTC, Rick O'Donnell. How much does a bullet cost? *Army Mag* 2002;**49**:49
3. Rao MC. Structure and properties of WO3 thin films for electrochromic device application. *J Non Oxide Glass* 2013;**5**:1–8
4. Keith LS, Moffett DB, Rosemond ZA, Wohlers DW, Agency for Toxic S, Disease R. ATSDR evaluation of health effects of tungsten and relevance to public health. *Toxicol Ind Health* 2007;**23**:347–87
5. *Criteria for a recommended standard: occupational exposure to tungsten and cemented tungsten carbide*. Washington, D.C.: NIOSH Publication and Products, 1977.
6. Keith LS, Wohlers DW, Moffett DB, Rosemond ZA, Agency for Toxic S, Disease R. ATSDR evaluation of potential for human exposure to tungsten. *Toxicol Ind Health* 2007;**23**:309–45
7. Tungsten chemical and their application, 2011, www.itia.info/assets/files/newsletters/Newsletter_2011_06.pdf (accessed 28 June 2016)
8. Sahle W, Krantz S, Christensson B, Laszlo I. Occupational exposure for tungsten oxide fibres, fibre-dose, during hard metal production. *Ann Occup Hyg* 1997;**41**:172–7
9. Aleksandr BS. Persistence of tungsten oxide particle/fiber mixtures in artificial human lung fluids. *Particle Fibre Toxicol* 2010;**7**:1–9
10. Guandalini GS, Zhang L, Fornero E, Centeno JA, Mokashi VP, Ortiz PA, Stockelman MD, Osterburg AR, Chapman GG. Tissue distribution of tungsten in mice following oral exposure to sodium tungstate. *Chem Res Toxicol* 2011;**24**:488–93
11. Scharf B, Clement CC, Wu XX, Morozova K, Zanolini D, Follenzi A, Larocca JN, Levon K, Sutterwala FS, Rand J, Cobelli N, Purdue E, Hajjar KA, Santambrogio L. Annexin A2 binds to endosomes following organelle destabilization by particulate wear debris. *Nat Commun* 2012;**3**:755
12. ITIA HSE Regulatory, www.itia.info/hse-regulatory.html (accessed 18 June 2016)
13. Bolt AM, Sabourin V, Molina MF, Police AM, Negro Silva LF, Plourde D, Lemaire M, Ursini-Siegel J, Mann KK. Tungsten targets the tumor microenvironment to enhance breast cancer metastasis. *Toxicol Sci* 2015;**143**:165–77
14. Lemus R, Venezia CF. An update to the toxicological profile for water-soluble and sparingly soluble tungsten substances. *Crit Rev Toxicol* 2015;**45**:388–411
15. NIOSH. NIOSH pocket guide to chemical hazards 2015, www.cdc.gov/niosh/npg/npgd0645.html (accessed 6 November 2015)
16. Bastian S, Busch W, Kuhnel D, Springer A, Meissner T, Holke R, Scholz S, Iwe M, Pompe W, Gelinsky M, Potthoff A, Richter V, Ikonomidou C, Schirmer K. Toxicity of tungsten carbide and cobalt-doped tungsten carbide nanoparticles in mammalian cells in vitro. *Environ Health Perspect* 2009;**117**:530–6
17. Koutsospyros A, Braida W, Christodoulatos C, Dermatas D, Strigul N. A review of tungsten: from environmental obscurity to scrutiny. *J Hazard Mater* 2006;**136**:1–19
18. Witten ML, Sheppard PR, Witten BL. Tungsten toxicity. *Chem Biol Interact* 2012;**196**:87–8
19. Madl AK, Pinkerton KE. Health effects of inhaled engineered and incidental nanoparticles. *Crit Rev Toxicol* 2009;**39**:629–58

20. Latz E, Xiao TS, Stutz A. Activation and regulation of the inflammasomes. *Nat Rev Immunol* 2013;**13**:397–411
21. Yazdi AS, Guarda G, Riteau N, Drexler SK, Tardivel A, Couillin I, Tschopp J. Nanoparticles activate the NLR pyrin domain containing 3 (Nlrp3) inflammasome and cause pulmonary inflammation through release of IL-1alpha and IL-1beta. *Proc Natl Acad Sci U S A* 2010;**107**:19449–54
22. Hornung V, Bauernfeind F, Halle A, Samstad EO, Kono H, Rock KL, Fitzgerald KA, Latz E. Silica crystals and aluminum salts activate the NALP3 inflammasome through phagosomal destabilization. *Nat Immunol* 2008;**9**:847–56
23. Lane T, Flam B, Lockey R, Kolliputi N. TXNIP shuttling: missing link between oxidative stress and inflammasome activation. *Front Physiol* 2013;**4**:50
24. Geoffrey MC. *The cell: a molecular approach*, 2nd edition. Sunderland, MA: Sinauer Associates, 2000
25. Fu PP, Xia Q, Hwang HM, Ray PC, Yu H. Mechanisms of nanotoxicity: generation of reactive oxygen species. *J Food Drug Anal* 2014;**22**:64–75
26. Lunov O, Syrovets T, Loos C, Nienhaus GU, Mailander V, Landfester K, Rouis M, Simmet T. Amino-functionalized polystyrene nanoparticles activate the NLRP3 inflammasome in human macrophages. *ACS Nano* 2011;**5**:9648–57
27. Tschopp J, Schroder K. NLRP3 inflammasome activation: the convergence of multiple signalling pathways on ROS production? *Nat Rev Immunol* 2010;**10**:210–5
28. Clogston JD, Patri AK. Zeta potential measurement. *Methods Mol Biol* 2011;**697**:63–70
29. OECD. *Test No. 403: acute inhalation toxicity*. Paris: OECD Publishing, 2009
30. Shvedova AA, Kisin E, Murray AR, Johnson VJ, Gorelik O, Arepalli S, Hubbs AF, Mercer RR, Keohavong P, Sussman N, Jin J, Yin J, Stone S, Chen BT, Deye G, Maynard A, Castranova V, Baron PA, Kagan VE. Inhalation vs. aspiration of single-walled carbon nanotubes in C57BL/6 mice: inflammation, fibrosis, oxidative stress, and mutagenesis. *Am J Physiol Lung Cell Mol Physiol* 2008;**295**:L552–65
31. Braakhuis HM, Gosens I, Krystek P, Boere JA, Cassee FR, Fokkens PH, Post JA, van Loveren H, Park MV. Particle size dependent deposition and pulmonary inflammation after short-term inhalation of silver nanoparticles. *Particle Fibre Toxicol* 2014;**11**:49
32. Rossi EM, Pylkkanen L, Koivisto AJ, Vippola M, Jensen KA, Miettinen M, Sirola K, Nykasenoja H, Karisola P, Stjernvall T, Vanhala E, Kiilunen M, Pasanen P, Makinen M, Hameri K, Joutsensaari J, Tuomi T, Jokiniemi J, Wolff H, Savolainen K, Matikainen S, Alenius H. Airway exposure to silica-coated TiO2 nanoparticles induces pulmonary neutrophilia in mice. *Toxicol Sci* 2010;**113**:422–33
33. Wong BA. Inhalation exposure systems: design, methods and operation. *Toxicol Pathol* 2007;**35**:3–14
34. Harbeck RJ. Immunophenotyping of bronchoalveolar lavage lymphocytes. *Clin Diagnos Labor Immunol* 1998;**5**:271–7
35. Labortories B-R. Protein blotting guide [PDF]. *Bio Rad Bull* 2015;**2895**:1–77
36. Sitapara RA, Antoine DJ, Sharma L, Patel VS, Ashby CR Jr., Gorasiya S, Yang H, Zur M, Mantell LL. The alpha7 nicotinic acetylcholine receptor agonist GTS-21 improves bacterial clearance in mice by restoring hyperoxia-compromised macrophage function. *Mol Med* 2014;**20**:238–47
37. Bonner JC. Nanoparticles as a potential cause of pleural and interstitial lung disease. *Proc Am Thor Soc* 2010;**7**:138–41
38. Pauwels NS, Bracke KR, Dupont LL, Van Pottelberge GR, Provoost S, Vanden Berghe T, Vandenabeele P, Lambrecht BN, Joos GF, Brusselle GG. Role of IL-1alpha and the Nlrp3/caspase-1/IL-1beta axis in cigarette smoke-induced pulmonary inflammation and COPD. *Eur RespirJ* 2011;**38**:1019–28
39. Ryman-Rasmussen JP, Tewksbury EW, Moss OR, Cesta MF, Wong BA, Bonner JC. Inhaled multiwalled carbon nanotubes potentiate airway fibrosis in murine allergic asthma. *Am J Respir Cell Mol Biol* 2009;**40**:349–58
40. Wang X, Xia T, Ntim SA, Ji Z, Lin S, Meng H, Chung CH, George S, Zhang H, Wang M, Li N, Yang Y, Castranova V, Mitra S, Bonner JC, Nel AE. Dispersal state of multiwalled carbon nanotubes elicits profibrogenic cellular responses that correlate with fibrogenesis biomarkers and fibrosis in the murine lung. *ACS Nano* 2011;**5**:9772–87
41. Hussain S, Sangtian S, Anderson SM, Snyder RJ, Marshburn JD, Rice AB, Bonner JC, Garantziotis S. Inflammasome activation in airway epithelial cells after multi-walled carbon nanotube exposure mediates a profibrotic response in lung fibroblasts. *Particle Fibre Toxicol* 2014;**11**:28
42. Roedel EQ, Cafasso DE, Lee KW, Pierce LM. Pulmonary toxicity after exposure to military-relevant heavy metal tungsten alloy particles. *Toxicol ApplPharmacol* 2012;**259**:74–86
43. Hussain SM, Warheit DB, Ng SP, Comfort KK, Grabinski CM, Braydich-Stolle LK. At the crossroads of nanotoxicology in vitro: past achievements and current challenges. *Toxicol Sci* 2015;**147**:5–16
44. Warheit DB. How meaningful are the results of nanotoxicity studies in the absence of adequate material characterization? *Toxicol Sci* 2008;**101**:183–5
45. Murdock RC, Braydich-Stolle L, Schrand AM, Schlager JJ, Hussain SM. Characterization of nanomaterial dispersion in solution prior to in vitro exposure using dynamic light scattering technique. *Toxicol Sci* 2008;**101**:239–53
46. Grassian VH, O'Shaughnessy PT, Adamcakova-Dodd A, Pettibone JM, Thorne PS. Inhalation exposure study of titanium dioxide nanoparticles with a primary particle size of 2 to 5 nm. *Environ Health Perspect* 2007;**115**:397–402
47. Creutzenberg O. Biological interactions and toxicity of nanomaterials in the respiratory tract and various approaches of aerosol generation for toxicity testing. *Arch Toxicol* 2012;**86**:1117–22
48. Srinivas Chinde ND, Mohammed Fazlur Rahmanan, Mohammed Mahboob, Rekhadevi Perumalla, Srinivas Indu Kumari, Paramjit Grover. Studies on toxicological assessment of tungsten oxide nanoparticles and microparticles in female wistar rats after acute oral exposure. In: *8th international nanotechnology conference*, Boston, 1–4 June 2016
49. Gillespie PA, Kang GS, Elder A, Gelein R, Chen L, Moreira AL, Koberstein J, Tchou-Wong KM, Gordon T, Chen LC. Pulmonary response after exposure to inhaled nickel hydroxide nanoparticles: short and long-term studies in mice. *Nanotoxicology* 2010;**4**:106–19
50. Phalen RF, Mannix RC, Drew RT. Inhalation exposure methodology. *Environ Health Perspect* 1984;**56**:23–34
51. Cantor JO, Osman M, Keller S, Cerreta JM, Mandl I, Turino GM. Measurement of cross-linked elastin synthesis in bleomycin-induced pulmonary fibrosis using a highly sensitive assay for desmosine and isodesmosine. *J Labor Clin Med* 1984;**103**:384–92
52. Cerreta JM. Amiodarone induced pulmonary fibrosis. In: Cantor J (ed.). *Handbook of animal models of pulmonary disease*. Vol. I, Boca Raton, FL: CRC Press, 1989, pp. 131–49
53. Cantor JO, Cerreta JM, Armand G, Osman M, Turino GM. The pulmonary matrix, glycosaminoglycans and pulmonary emphysema. *Connect Tissue Res* 1999;**40**:97–104
54. Bhavsar TM, Cantor JO, Patel SN, Lau-Cam CA. Attenuating effect of taurine on lipopolysaccharide-induced acute lung injury in hamsters. *Pharmacol Res* 2009;**60**:418–28
55. Bhavsar T, Liu M, Hardej D, Liu X, Cantor J. Aerosolized recombinant human lysozyme ameliorates Pseudomonas aeruginosa-induced pneumonia in hamsters. *Exp Lung Res* 2010;**36**:94–100
56. Bhavsar T, Liu M, Liu X, Cantor J. Aerosolized recombinant human lysozyme enhances the bactericidal effect of tobramycin in a hamster model of Pseudomonas aeruginosa-induced pneumonia. *Exp Lung Res* 2011;**37**:536–41
57. Gordon T, Bosland M. Strain-dependent differences in susceptibility to lung cancer in inbred mice exposed to mainstream cigarette smoke. *Cancer Lett* 2009;**275**:213–20
58. Scoville DK, White CC, Botta D, McConnachie LA, Zadworny ME, Schmuck SC, Hu X, Gao X, Yu J, Dills RL, Sheppard L, Delaney MA, Griffith WC, Beyer RP, Zangar RC, Pounds JG, Faustman EM, Kavanagh TJ. Susceptibility to quantum dot induced lung inflammation differs widely among the collaborative cross founder mouse strains. *Toxicol Appl Pharmacol* 2015;**289**:240–50
59. Corteling R, Wyss D, Triefilieff A. In vivo models of lung neutrophil activation. Comparison of mice and hamsters. *BMC Pharmacol* 2002;**2**:1

60. Kang GS, Gillespie PA, Gunnison A, Moreira AL, Tchou-Wong KM, Chen LC. Long-term inhalation exposure to nickel nanoparticles exacerbated atherosclerosis in a susceptible mouse model. *Environ Health Perspect* 2011;**119**:176–81
61. Ware LB, Matthay MA. The acute respiratory distress syndrome. *N Engl J Med* 2000;**342**:1334–49
62. Wang CC, Wang S, Xia Q, He W, Yin JJ, Fu PP, Li JH. Phototoxicity of zinc oxide nanoparticles in HaCaT keratinocytes-generation of oxidative DNA damage during UVA and visible light irradiation. *J Nanosci Nanotechnol* 2013;**13**:3880–8
63. Ding LR, Wang K, Fahmy B, Shen HH, Cormier S. Airborne fine particulate matter induced pulmonary inflammation as well as oxidative stress in neonate rats. *Chin Med J* 2010;**123**:2895–900
64. Mantecca P, Farina F, Moschini E, Gallinotti D, Gualtieri M, Rohr A, Sancini G, Palestini P, Camatini M. Comparative acute lung inflammation induced by atmospheric PM and size-fractionated tire particles. *Toxicol Lett* 2010;**198**:244–54
65. Srinivas A, Rao PJ, Selvam G, Murthy PB, Reddy PN. Acute inhalation toxicity of cerium oxide nanoparticles in rats. *Toxicol Lett* 2011;**205**:105–15
66. Fehrenbach H. Alveolar epithelial type II cell: defender of the alveolus revisited. *Respir Res* 2001;**2**:33–46
67. Rubins JB. Alveolar macrophages: wielding the double-edged sword of inflammation. *Am J Respir Crit Care Med* 2003;**167**:103–4
68. Suzuki Y, Churg J, Ono T. Phagocytic activity of the alveolar epithelial cells in pulmonary asbestosis. *Am J Pathol* 1972;**69**:373–88
69. Oberdorster G. Safety assessment for nanotechnology and nanomedicine: concepts of nanotoxicology. *J Int Med* 2010;**267**:89–105
70. Rydman EM, Ilves M, Vanhala E, Vippola M, Lehto M, Kinaret PA, Pylkkanen L, Happo M, Hirvonen MR, Greco D, Savolainen K, Wolff H, Alenius H. A single aspiration of rod-like carbon nanotubes induces asbestos-like pulmonary inflammation mediated in part by the IL-1 receptor. *Toxicol Sci* 2015;**147**:140–55
71. Li Z, Berk M, McIntyre TM, Gores GJ, Feldstein AE. The lysosomal-mitochondrial axis in free fatty acid-induced hepatic lipotoxicity. *Hepatology* 2008;**47**:1495–503
72. Akhtar MJ, Ahamed M, Kumar S, Siddiqui H, Patil G, Ashquin M, Ahmad I. Nanotoxicity of pure silica mediated through oxidant generation rather than glutathione depletion in human lung epithelial cells. *Toxicology* 2010;**276**:95–102
73. Shukla RK, Sharma V, Pandey AK, Singh S, Sultana S, Dhawan A. ROS-mediated genotoxicity induced by titanium dioxide nanoparticles in human epidermal cells. *Toxicol In Vitro* 2011;**25**:231–41
74. Paget V, Moche H, Kortulewski T, Grall R, Irbah L, Nesslany F, Chevillard S. Human cell line-dependent WC-Co nanoparticle cytotoxicity and genotoxicity: a key role of ROS production. *Toxicol Sci* 2015;**143**:385–97
75. Kondapalli S. *Tungsten oxide nanoparticles induce oxidative stress and apoptosis in Rat pleural mesothelial cells*. Queens, NY: St. John's University, 2015
76. Lamkanfi M, Sarkar A, Vande Walle L, Vitari AC, Amer AO, Wewers MD, Tracey KJ, Kanneganti TD, Dixit VM. Inflammasome-dependent release of the alarmin HMGB1 in endotoxemia. *J Immunol* 2010;**185**:4385–92
77. Yang H, Wang H, Czura CJ, Tracey KJ. The cytokine activity of HMGB1. *J Leukoc Biol* 2005;**78**:1–8
78. de Zoete MR, Palm NW, Zhu S, Flavell RA. Inflammasomes. *Cold Spring Harb Perspect Biol* 2014;**6**:a016287
79. Vanwinkle BA, de Mesy Bentley KL, Malecki JM, Gunter KK, Evans IM, Elder A, Finkelstein JN, Oberdorster G, Gunter TE. Nanoparticle (NP) uptake by type I alveolar epithelial cells and their oxidant stress response. *Nanotoxicology* 2009;**3**:307–18
80. Pelegrin P, Surprenant A. Dynamics of macrophage polarization reveal new mechanism to inhibit IL-1beta release through pyrophosphates. *EMBO J* 2009;**28**:2114–27

(Received April 4, 2016, Accepted July 26, 2016)